Observations of a Large-Amplitude Internal Wave Train and Its Reflection off a Steep Slope

DANIEL BOURGAULT

Institut des Sciences de la Mer de Rimouski, Rimouski, Quebec, Canada

DAVID C. JANES

Memorial University, St. John's, Newfoundland and Labrador, Canada

PETER S. GALBRAITH

Department of Fisheries and Oceans Canada, Mont-Joli, Quebec, Canada

ABSTRACT

Remote and in situ field observations documenting the reflection of a normally incident, short, and large-amplitude internal wave train off a steep slope are presented and interpreted with the help of the Dubreil–Jacotin–Long theory. Of the seven remotely observed waves that composed the incoming wave train, five were observed to reflect. It is estimated that the incoming wave train carried $E_i = (24 \pm 4) \times 10^4$ J m^{-1} to the boundary. The reflection coefficient, defined as the ratio of reflected to incoming wave train energies, is estimated to be $R = 0.5 \pm 0.2$. This is about 0.4 lower than parameterizations in the literature, which are based on reflections of single solitary waves, would suggest. It is also shown that the characteristics of the wave-boundary situation observed in the field are outside the parameter space examined in previous laboratory and numerical experiments on internal solitary wave reflectance. This casts doubts on extrapolating current laboratory-based knowledge to fjord-like systems and calls for more research on internal solitary wave reflectance.

1. Introduction

In idealized two-layer systems, when a first-mode internal solitary wave of depression approaches normally a uniformly shoaling bottom, or "internal beach," a fraction R of its energy reflects into first-mode internal waves. The remaining energy induces other motions (e.g., boluses, swash, intrusion, etc.), is dissipated in the bottom boundary, or is converted to turbulence during wave breaking and run up. Exactly how the incident wave energy is partitioned among these processes (and, more specifically, what fraction is reflected) is not fully understood. Understanding these processes is needed to assess the suspected importance of wave-induced boundary processes in coastal mixing (Bourgault and Kelley 2003; Boegman et al. 2005a;

Helfrich and Melville 2006; Scotti and Pineda 2004; Bourgault et al. 2005, 2007, 2008; Moum et al. 2007a,b).

Our understanding of the reflection of internal solitary waves is partly based on idealized laboratory experiments (Wallace and Wilkinson 1988; Helfrich 1992; Michallet and Ivey 1999; Boegman et al. 2005b; Chen et al. 2007). However, the applicability of the laboratory-based results to ocean situations has recently been questioned by results of numerical experiments. Bourgault and Kelley (2007) revisited, with two-dimensional numerical simulations, the laboratory findings of Michallet and Ivey (1999) for the reflectance property of smooth boundaries of constant slope on normally incident and laminar internal solitary waves. They concluded that the reflectance measured in the laboratory was underestimated, by approximately 0.1, because of friction along the sidewalls of the tank, an aspect that was not taken into account by Michallet and Ivey (1999). Bourgault and Kelley (2007) proposed the following empirically based parameterization for the reflectance without sidewall effects:

Corresponding author address: Daniel Bourgault, Institut des Sciences de la Mer de Rimouski, 310 Allée des Ursulines, C.P. 3300, Rimouski QC G5L 3A1, Canada.
E-mail: daniel_bourgault@uqar.ca

$$R_{BK} \equiv \frac{E_r}{E_i} = 1 - e^{-\xi/\xi_0}, \qquad (1)$$

where E_r and E_i are the reflected and incoming wave energies, respectively; $\xi_0 = 0.78 \pm 0.02$; and

$$\xi = \frac{s}{(a/L)^{1/2}} \qquad (2)$$

is the Iribarren number (Boegman et al. 2005b), where s is the bottom slope and

$$L = \frac{1}{a} \int_{-\infty}^{\infty} |\eta_{max}| \, dx \qquad (3)$$

is the horizontal length scale of the incoming wave. Here η_{max} is the excursion of the isopycnal undergoing maximum displacement and a is the maximum displacement of that isopycnal, or wave amplitude.

Lamb and Nguyen (2009), also using two-dimensional numerical simulations, in turn revisited the results of Bourgault and Kelley (2007) as well as the assumption of equipartition of kinetic and available potential energy fluxes often made for calculating wave energy (as done, e.g., in Helfrich 1992; Michallet and Ivey 1999; Bourgault and Kelley 2007). They found that this assumption can lead to a 0.1 overestimation of reflectance for cases where the pycnocline is close to the surface. They also found that reflectance depends on the Reynolds number that characterizes the incident wave and therefore questioned the relevance of using the Iribarren number for parameterizing wave-slope reflectance. They concluded that, although the parameterization in (1) may be adequate for low Reynolds number situations typical of laboratory settings, it should be used cautiously when applied to oceanographic conditions where Reynolds numbers are typically orders of magnitude higher.

But how cautious should we be? There are few reports of field measurements to provide guidance in this matter. To date, estimates of natural slope reflectance have mostly relied on extrapolating laboratory-scale findings to field situations. This approach has been used, for example, by Michallet and Ivey (1999, their Table 2), Bourgault and Kelley (2003), Bourgault et al. (2007), and Boegman et al. (2005a, their Table 2) to characterize the reflectance and mixing properties of a number of coastal ocean slopes. One exception is the interpretation that Boegman et al. (2005a) made of temperature time series observations from Lake Pusiano. Based on similarities of the observed signal to results of a laboratory experiment on the degeneration of internal seiches, they estimated reflection coefficients to be within the uncertainties of the laboratory measurements of Michallet and Ivey (1999).

Here we present further field evidence documenting the reflection of a large-amplitude internal solitary wave train off a steep internal beach in a fjord. The observations are interpreted with the help of the Dubreil–Jacotin–Long (DJL) theory from which wave train structure and reflectance are estimated. The results are discussed in the context of laboratory-scale studies upon which our understanding of internal wave reflectance is currently based. We conclude with recommendations on extrapolating current laboratory-based and numerically based results to natural slopes and provide suggestions for future research.

2. Field experiment

Measurements were collected in the Saguenay Fjord, Quebec (Fig. 1), between 1650 and 1905 UTC 5 July 2007. Sampling took place roughly between 0 and 2 h after the time of low water (1711 UTC) at the mouth [Tadoussac (T)].

The Saguenay fjord is 120 km long and 2 km wide on average. From mouth to head, the bottom topography is characterized by three sills: a shallow (30 m) sill at the mouth, an intermediate (60 m) sill 20 km up fjord (Fig. 1), and a deep (120 m) sill 30 km up fjord. These sills separate three basins of depths varying between 180 and 280 m. During summer conditions, a mean freshwater input rate of 1200 m^3 s^{-1} from the Saguenay River mixes with saltwater to induce an estuarine-like circulation principally modulated by the M_2 tide with amplitude of 1.6 m at the mouth (Stacey and Gratton 2001; Bélanger 2003).

Sampling took place near the intermediate sill (Fig. 1), which we hypothesized to be a wave generation site, based on preliminary observations collected the year before and on the modeling study of Janes (2008). Sampling was carried out from an 8-m scientific boat, the *Krill*. The sampling strategy was to visually search around the sill for sea surface banded patterns typical of those induced by internal waves in similar environments (e.g., Farmer and Armi 1999; Bourgault and Kelley 2003; Cummins et al. 2003). When a potential wave train was located, the *Krill* was positioned ahead of the banded pattern and left to drift while sampling was carried out with the instruments described next.

Fine-structure flow visualization and three-dimensional current profiles were obtained with an RD Instruments Workhorse 600-kHz acoustic Doppler current profiler (ADCP). The ADCP recorded internally with no real-time display of the measurements. Sampling strategy and decisions solely relied on sea surface signatures. The ADCP pinging and record rate was 1 Hz, the vertical bin size was 0.25 m, and the range was 27 m. While drifting, the ADCP was hung on a rope over the side of the boat at about 1 m below the sea surface. The sea surface was flat
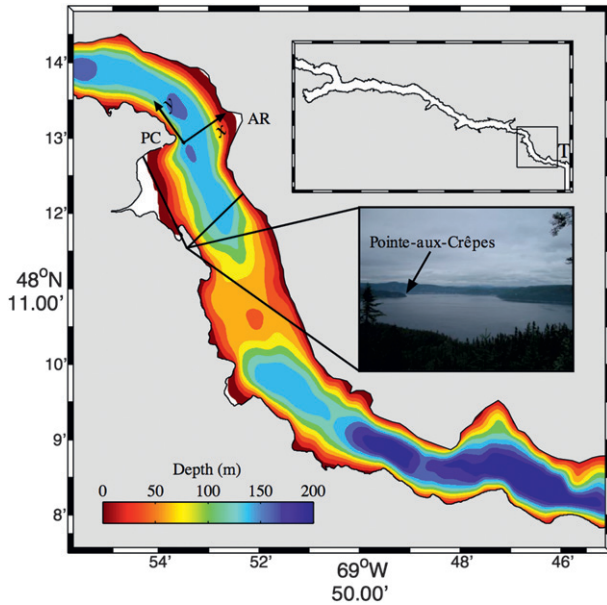
FIG. 1. Bathymetric chart and sample picture of the field site around the intermediate sill in the Saguenay Fjord. This bathymetric dataset was linearly interpolated on a 50-m-resolution grid from the isobaths and depth soundings manually digitized from the Canadian Hydrographic Service nautical chart 1203. The oblique black lines indicate the field of view of the camera. The orthogonal vectors, labeled x and y, represent the coordinate system used for current measurements presented in Fig. 4. The origin of this coordinate system coincides with the location where data presented in Figs. 4 and 5 were collected. The location of Pointe-aux-Crêpes (PC), Anse-de-Roche (AR), and the town of Tadoussac (T) at the mouth of the fjord are shown.

calm when the observations were collected and the pitch and roll of the ADCP stayed within ±6°. The current measurements were ground-referenced by adding the boat's drift velocity, determined with a global positioning system (GPS) unit. To reduce random noise, the ADCP measurements were binned into 20-s ensemble averages and 1-m vertical bin sizes. The velocity uncertainty in the binned data is ±0.05 m s^{-1}.

While the *Krill* was drifting over an internal wave train, individual profiles of pressure, temperature, conductivity, and vertical shear were collected with a free-fall, loosely tethered, coastal vertical microstructure profiler (VMP) manufactured by Rockland Scientific International. This is the same instrument as used in Bourgault et al. (2008) from which 1-m-scale dissipation rates of turbulent kinetic energy (W kg^{-1}) were calculated as

$$\epsilon = \frac{15}{2} \nu \overline{(u_z)^2},$$ (4)

where u_z is the measured microstructure vertical shear, excluding instrumental noise. We refer to standard

publications for more details on the methods for calculating ϵ (Oakey and Elliott 1982; Wesson and Gregg 1994; Moum et al. 1995; Peters 1997). Note that shear measurements u_z depend on the flow speed past the shear probes, which is generally assumed to be equal to the fall speed of the profiler (Macoun and Lueck 2004). However, this assumption does not hold when sampling through phenomena like internal waves characterized with vertical velocities comparable to the fall speed of the profiler (see also Klymak and Gregg 2004). To compensate for this, the vertical velocity from the ADCP was used to calculate the flow speed past the shear probes, as described in Bourgault et al. (2008).

In calculating ϵ, it is assumed that turbulence is isotropic at small scales (e.g., Thorpe 2005). However, Gargett et al. (1984) concluded that the isotropic assumption may be violated if $\epsilon/(\nu N^2)$ is less than 200, where $\nu \approx 10^{-6}$ m^2 s^{-1} is the molecular kinematic viscosity and

$$N^2 = -\frac{g}{\rho_0} \rho_z$$ (5)

is the square of the buoyancy frequency, calculated over 1-m scale, to match the ϵ data, and from the Thorpe-sorted density ρ, reference density $\rho_0 = 1023$ kg m^{-3}, and gravitational acceleration $g = 9.81$ m s^{-2} (for a review on this subject, see Thorpe 2005). Of all measurements collected during this experiment, 82% satisfies the isotropy criterion [i.e., $\epsilon/(\nu N^2) > 200$]. The remaining 18% was flagged and will be identified in figures. According to Denman and Gargett (1988), the dissipation rate for those anisotropic data segments may be overestimated by a factor of 3.

Finally, shore-based photography (Fig. 1) was collected to obtain information on the spatiotemporal variability of surface signatures of internal waves. Time-lapse photographs were collected every 60 s with a 7.1-megapixel Canon Powershot S70 camera. The camera was located on a 100-m-elevation hill at 48°11.530′N, 69°53.430′W (Fig. 1). The field of view is roughly toward north. Images were georectified following Pawlowicz (2003) and Bourgault (2008) using natural landmarks as well as the *Krill* as ground control points. Specific details about the georectification can be found in Janes (2008). The root-mean-square difference between the ground control points (15 were used) and the georectified points is 54 m. This indicates that the position uncertainty of the georectified images is ±27 m. This systematic error tends to cancel out for distance measurements. The error in measuring distances is dominated by the effective footprint length scale taken as

$$\Delta = \sqrt{(\Delta x_p)^2 + (\Delta y_p)^2},$$ (6)

where Δx_p and Δy_p are the eastward and northward distances between adjacent georectified pixels, respectively (Fig. 2). Because a feature in the georectified images can be located to within $\pm\Delta/2$, the uncertainty in distance measurements is $\delta d = \pm\Delta$.

3. Observations

a. Wave train propagation and background conditions

At 1738 UTC, the *Krill* was positioned just off Pointe-aux-Crêpes (PC) in front of a series of sea surface bands typical of those induced by internal waves (Fig. 3, left). The bands extended across the entire width of the fjord and their propagation direction, at the location of the *Krill*, was $\theta = 35° \pm 5°$ anticlockwise from north. The in situ observations revealed that the bands were indeed coincident with an internal wave train (Figs. 4, 5). The horizontal current measurements (Fig. 4), originally collected in the earth geographic coordinates, were rotated anticlockwise by 35° to obtain across-wave u and along-wave v propagation currents (see coordinate system in Fig. 1). The along-wave propagation current v above wave troughs is positive, consistent with up-fjord-propagating internal solitary waves of depression. The pattern of the vertical currents is consistent with that of first-mode internal solitary waves of depression.

The phase speed of the waves at the location of the in situ measurements could not unambiguously be measured from the shore-based photography. For unknown reasons, there is a quasi absence of wave-like sea surface patterns in the image just off Pointe-aux-Crêpes, where the in situ observations were collected (Fig. 3, left). The sea surface signature of the waves is however clear a few hundred meters toward the middle of the channel. The phase speeds were determined by interpolating the pixel intensities in a space–time coordinate system taken along the midchannel axis shown in Fig. 3. The wave train phase speed is around $c = 0.5$ m s^{-1}, without significant difference between the individual waves that composed the wave train (Fig. 6, bottom).

The leading wave is asymmetrical with an amplitude of 13 ± 2 m, as determined visually from the echogram (Fig. 4). The following two waves have roughly the same amplitudes of 6 ± 1 m. High levels of dissipation rates are coincident with the leading wave in comparison to the rest of the observations (Fig. 4, profile 2). For this profile, the dissipation rates averaged over the first 14 m is $\overline{\epsilon}_{14m} = 1.2 \times 10^{-4}$ W kg^{-1}. By comparison, the rest of the measurements are characterized with $\overline{\epsilon} = 3.3(15, 0.019) \times 10^{-6}$ W kg^{-1}, where the numbers in parentheses are the 2.5 and 97.5 percentiles of the
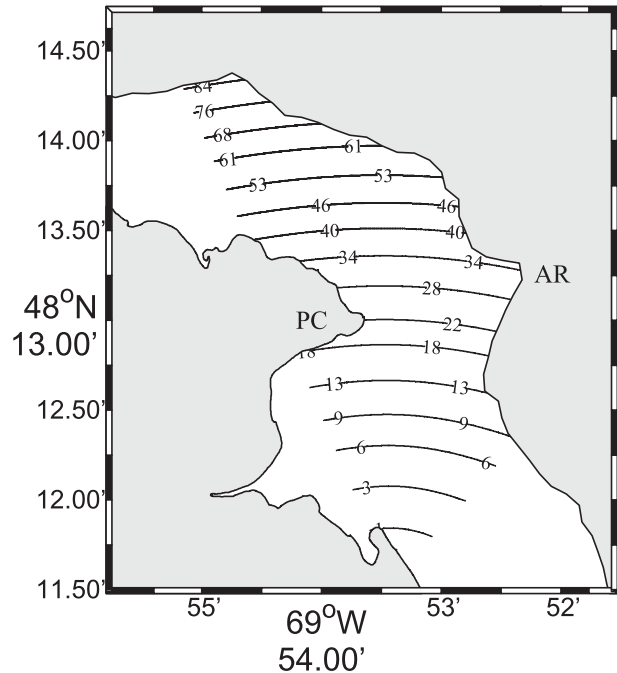

FIG. 2. Effective pixel resolution Δ (m) of the georectified images. Phase speed measurements presented in section 3 (see Fig. 6 and Tables 1, 2) were taken from the southern flank of PC, where the resolution is 13 m $< \Delta <$ 18 m. This is about $^{1}/_{3}$ of inferred wave horizontal length scales L (see Table 1).

distribution. The turbulent core of the leading wave is also characterized with density overturns (Fig. 5, profile 2). The largest of these overturns, located between 9.5 and 13.7 m, is characterized with a Thorpe scale $L_T = 1.8$ m and available potential energy density $P = 1.3 \times 10^{-3}$ J kg^{-1} (Galbraith and Kelley 1996). The second largest overturn, between 5.6 and 6.7 m, is characterized with $L_T = 0.54$ m and $P = 0.16 \times 10^{-3}$ J kg^{-1}. These observations suggest that the leading wave is breaking.

Only the first three waves could be sampled once before being forced to leave the site to yield passage to a commercial ship. We then moved the *Krill* farther upstream and closer to the eastern shore, again in front of a series of sea surface banded features (Fig. 3, right). During data analysis, the georectified images revealed that we had sampled, without realizing it while at sea, another portion of the same wave train we had sampled a few minutes earlier off Pointe-aux-Crêpes. The leading wave had an amplitude of around 5 m (Fig. 7), much smaller than the leading wave observed off Pointe-aux-Crêpes (Fig. 4). The georectified images (Fig. 3) and animation (not shown) show that as the wave train propagated up fjord it tended to follow the channel's curvature.

The background currents U and V (Fig. 8) in which the wave train evolved were determined by computing a 60-s average of u and v, from 1738 to 1739 UTC, which
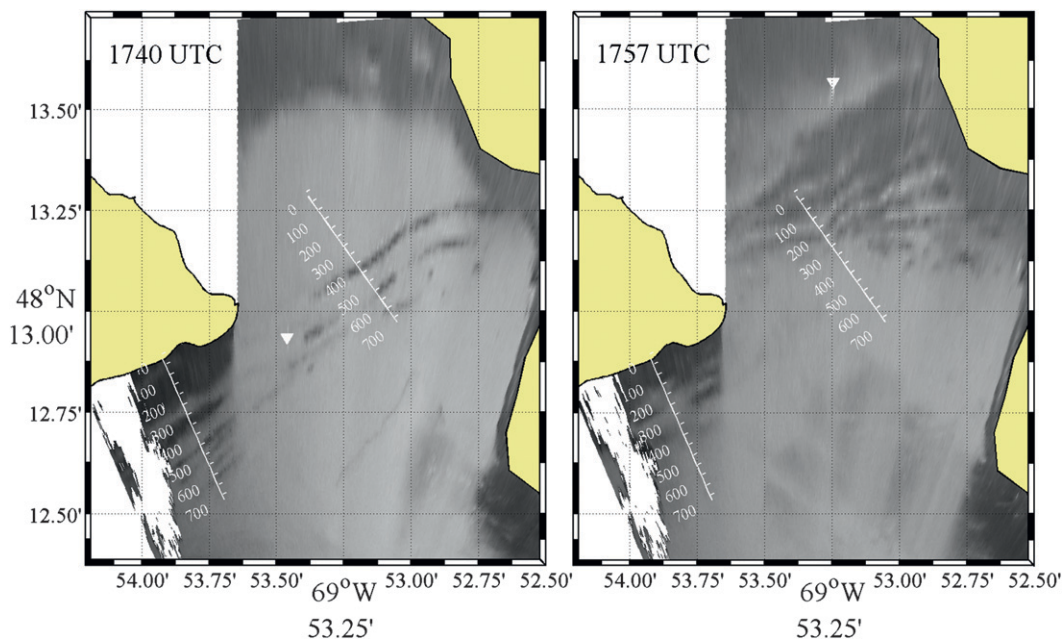
FIG. 3. Sea surface signature of the internal wave train around (left) 1740 and (right) 1757 UTC 5 Jul 2007. See Figs. 4 and 7 for corresponding in situ observations. The white triangles indicate the *Krill* position. The white 700-m-long scales extending off the flank of PC and in the middle of the channel are the transects along which space–time representations of the photographs are presented in Fig. 6.

corresponds to the data available prior to the arrival of the leading wave. The main pycnocline (<5 m) appears to be dynamically stable with a minimum Richardson number

$$\text{Ri} = \frac{N^2}{U_z^2 + V_z^2} \approx 0.5: \tag{7}$$

that is, greater than the theoretical criterion ($>\frac{1}{4}$) for dynamic instability (Miles 1961).

b. Wave train reflection

As the wave train propagated, its northeastern section continued up fjord, with indications of wave refraction in Anse-de-Roche (AR; Fig. 3), while its southwestern section collided and reflected off the southern flank of Pointe-aux-Crêpes (Fig. 9). Of the seven incoming bands, four are seen to have reflected. This suggests that the individual waves that formed the incoming wave train interacted and combined during reflection. This is seen, for example, in the laboratory experiments of Helfrich (1992, his Fig. 18) and Boegman et al. (2005a, their Fig. 4c) where multiple incident waves may produce fewer reflected waves. Another possibility is that some of the reflected waves were too small to be detected with our camera.

Another perspective of the wave-boundary interaction is obtained by interpolating the pixel intensities in a space–time coordinate system taken orthogonal to wave crests and extending off the flank of Pointe-aux-Crêpes

(Fig. 6). In this representation, the wave reflection event appears as a series of "V" patterns, or wave rays, seen between 1730 and 1815 UTC. The incoming and reflected wave trains are composed of 7 and 5 rays, respectively, consistent with the number of surface bands, although the fifth reflected wave was not clearly identified in Fig. 9. Another series of about seven incoming wave rays is also seen around 1845 UTC, but the camera was stopped before evidence of wave reflection could be seen.

There is no evidence of the waves slowing down as they approach the coast. Similar observations were reported by Bourgault et al. (2007) for an internal solitary wave shoaling on a much gentler slope (3° relative to 30°) in the St. Lawrence Estuary. Their observations (their Figs. 2, 4) showed that the phase speed remained constant, to within data uncertainties, up to the turning point, even though the depth changed from about 30 to 20 m. Presumably, the amplitude growth compensates for the decreasing depth on the phase speed.

The phase speeds c of the incoming and reflected waves were determined by manually digitizing each ray. The ray slopes, and thus phase speeds, were determined with linear least squares fits. The phase speeds of the incoming and reflected waves are listed in Tables 1 and 2, respectively. The uncertainties provided are the 95% confidence intervals of the fitted slopes. The phase speeds of the waves approaching the southern flank of Pointe-aux-Crêpes are significantly larger than the phase speeds of
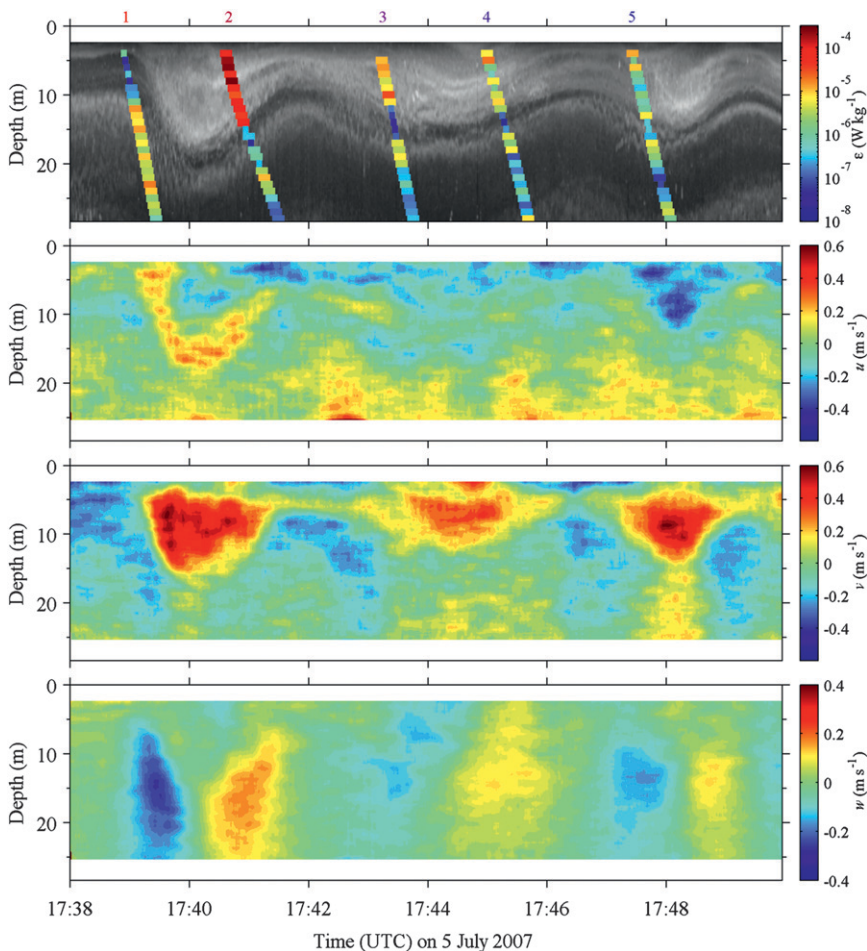
FIG. 4. In situ observations of the internal wave train observed off PC (see Fig. 3, left). Space–time contours of (top)–(bottom) the 4-beam average backscatter intensity corrected for radial spreading (grayscale, arbitrary units), across-wave current u, along-wave current v, and vertical current w. The horizontal currents u and v are relative to the wave propagation direction $\theta = 35°$ anticlockwise from north as determined from shore-based photography (see text and Figs. 1, 3) Shown in (top) are also profiles (color) of the dissipation rates of turbulent kinetic energy ϵ. The thinner segments in the ϵ profiles are those that failed the isotropy criterion $\epsilon/(\nu N^2) > 200$ (see section 2). These may be overestimated by a factor of 3. The color-coded numbers 1–5 above (top) are identification labels for the VMP profiles for comparison with Fig. 5.

the wave train in midchannel (cf. the ray slopes in Fig. 6). We attribute this difference as an indication that waves approaching the southern flank of Pointe-aux-Crêpes are sheltered from the facing current, a point further discussed below.

4. Theory

a. Theory description

Given the lack of in situ measurements for the portion of the wave train approaching and reflecting off the southern flank of Pointe-aux-Crêpes, we rely on the inviscid, fully nonlinear, steady-state, two-dimensional DJL theory to

infer wave characteristics and energies from observed background conditions and phase speeds. The DJL nonlinear wave equation with background current can be written as (Stastna and Lamb 2002)

$$\nabla^2 \eta + \frac{V'(z - \eta)}{c - V(z - \eta)}[\eta_x^2 + (\eta_z - 2)\eta_z]$$
$$+ \frac{N^2(z - \eta)}{[c - V(z - \eta)]^2}\eta = 0, \qquad (8)$$

where $\eta(x, z)$ is the isopycnal displacement, c is the wave phase speed, $V(z)$ is the background current, and $N(z)$ is the background buoyancy frequency. Along
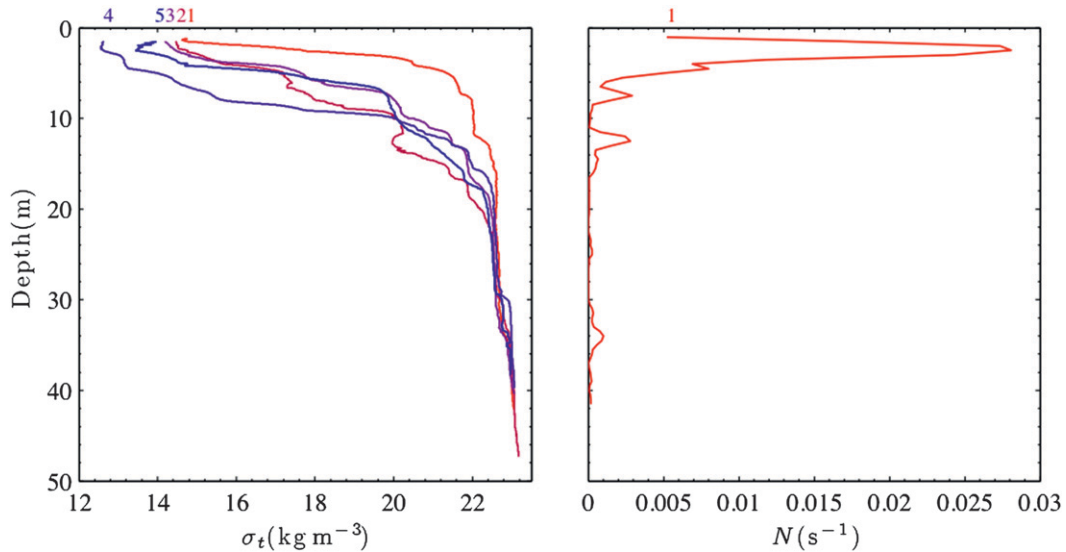
FIG. 5. (left) Density profiles collected through the wave train of Fig. 4 and (right) 0.5-m scale buoyancy frequency N of profile 1. The pycnocline is located at depth $h_1 = 2.5$ m and is characterized with $N = 0.028$ s^{-1}. The color-coded numbers 1–5 above the figure are identification labels for comparison with Fig. 4.

with boundary conditions (i.e., $\eta = 0$ at surface, bottom, and $\pm\infty$) and imposed available potential energy, Eq. (8) is solved numerically following algorithms described in Turkington et al. (1991) and Stastna and Lamb (2002)

with a source code provided by K. G. Lamb (University of Waterloo, 2009, personal communication) modified to handle discrete field measurements. Once a solution for η and c is obtained, the density field ρ as well as the
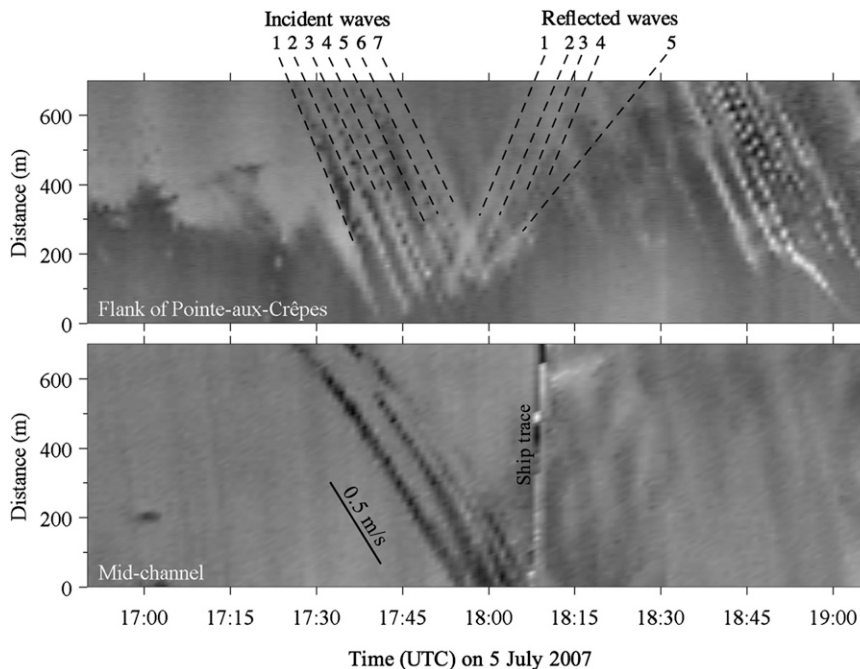

FIG. 6. Internal wave rays seen from a space–time representation of the georectified pho-tographs interpolated along (top) an axis extending off the southern flank of PC and (bottom) a midchannel axis (see Fig. 3). The numbered dashed lines in (top) are visual aids to help identify incoming and reflected wave rays.
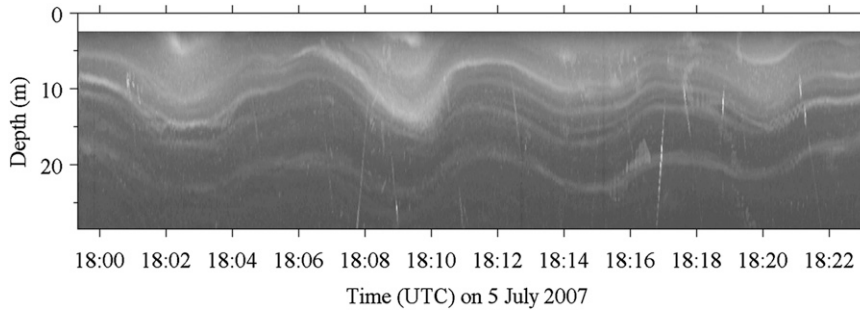
FIG. 7. Echogram (arbitrary units) of the internal wave train observed the second time in the middle of the channel (see Fig. 3, right).

horizontal and vertical currents, u and w, can be determined from the streamfunction of the wave-induced motion (for details, see Lamb 2002; Stastna and Lamb 2002).

b. Theory/data comparison

1) MODEL SETUP

With some extrapolation to compensate for the observational gap of the background conditions, the DJL theory described above can be compared with field observations. To achieve this, Eq. (8) is solved on a numerical domain that is 600 m long (i.e., about 10 times the expected wave horizontal length scale) and 150 m deep (i.e., the total depth where the in situ observations were

collected). The horizontal and vertical grid sizes are $\Delta x = 1$ m and $\Delta z = 0.2$ m, respectively. Two simulations were carried out: one matching the amplitude of the second wave of Fig. 4 ($a \simeq 6$ m) and one matching the amplitude of the leading wave ($a \simeq 13$ m).

The background density profile, and thus N in Eq. (8), is taken from the observations collected just ahead of the wave train (profile 1 in Figs. 4, 5). The profile is extrapolated below observational depth (i.e., below 47 m) with the function

$$\rho(z < -47\,\text{m}) = ae^{b/(z+c)}, \tag{9}$$

where $a = 1024.73$ kg m^{-3}, $b = 0.06481$ m, and $c = -4.415$ m (Fig. 10). These coefficients were determined
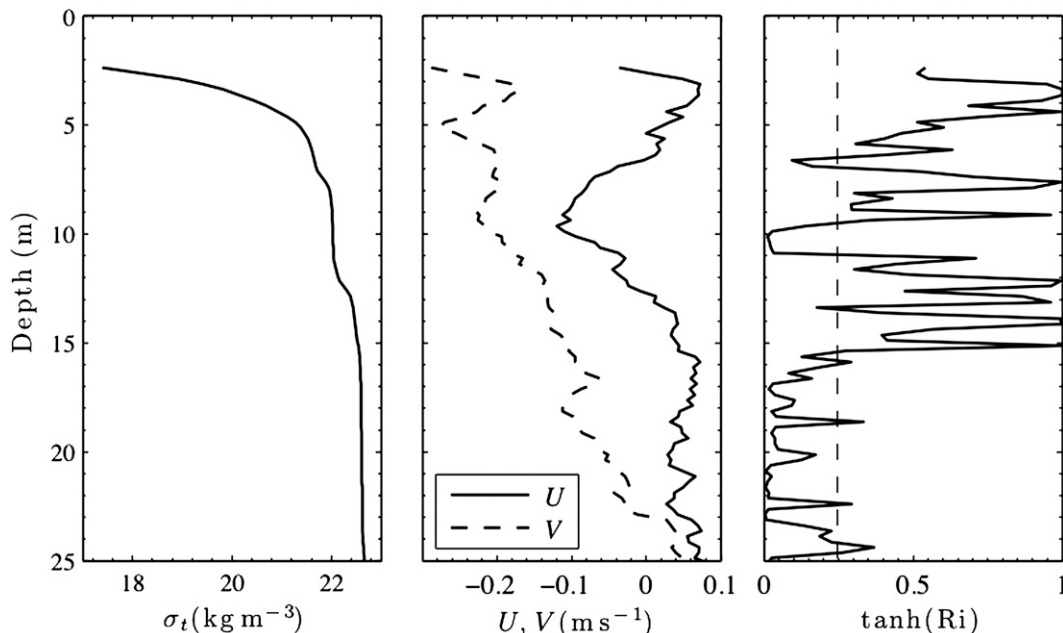

FIG. 8. Background conditions off PC prior to the passage of the wave train of Fig. 4: (left) 1-m-scale density profile just ahead of the leading wave (profile 1 in Figs. 4, 5); (middle) 1-m-scale and 60-s-average across-wave (U) and along-wave (V) current; and (right) 1-m-scale Richardson number with the dashed line located at the critical value $\text{Ri}_c = \frac{1}{4}$.
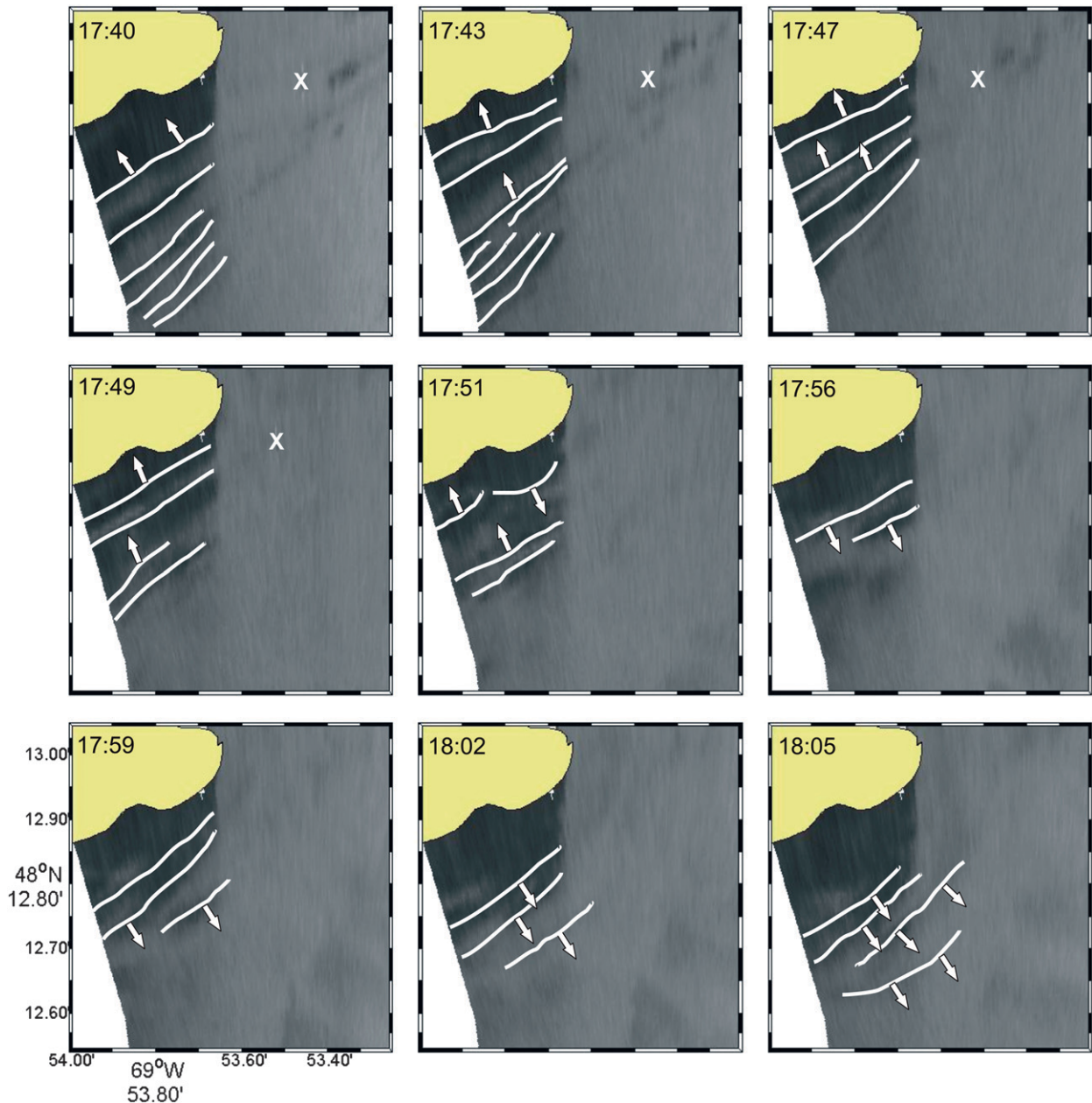
FIG. 9. Sequence of georectified photographs showing the wave train progression as it collided and reflected off the southern flank of PC. Vectors only indicate propagation direction. The time is in UTC.

from a least squares fit to 28 historical density profiles collected in the vicinity of the intermediate sill for summer periods between 1988 and 2007. The data were extracted from the Oceanographic Data Management System, Fisheries and Oceans Canada.

The background current V in the first 25 m is taken from field measurements. Below, the background current was extrapolated using results from a laterally averaged, nonhydrostatic numerical circulation model of the fjord. The model is described in Bourgault and Kelley (2004)

and was implemented with realistic bathymetry to the fjord by Janes (2008). Simulations were idealized with an initial background two-layer density profile and M_2 tidal forcing at the mouth. The vertical current structure at around the same location and tidal phase as the observations presented here were extracted and used to extrapolate the background current measurements below 25 m (Fig. 10). The main results presented below are not significantly sensitive to ± 0.1 m s^{-1} perturbations added to this extrapolation.

TABLE 1. Characteristics of each wave of the incoming wave train (Fig. 6) as inferred from the DJL theory given phase speed measurements and background density profile. The uncertainties in a, L, E_i, and related quantities stem from phase speed uncertainties. See text for definition of variables.

No.	c (m s^{-1})	a (m)	L (m)	α	λ	ξ	R_{BK}	E_i ($\times 10^4$ J m^{-1})
1	0.69 ± 0.04	5.2 ± 0.4	44.5 ± 0.2	2.1	0.6	1.6 ± 0.1	0.87 ± 0.03	7 ± 1
2	0.68 ± 0.02	5.0 ± 0.2	44.6 ± 0.2	2.0	0.6	1.7 ± 0.1	0.88 ± 0.02	6.0 ± 0.4
3	0.60 ± 0.02	3.2 ± 0.2	52 ± 2	1.3	0.7	2.2 ± 0.2	0.94 ± 0.02	2.5 ± 0.3
4	0.62 ± 0.03	3.5 ± 0.3	50 ± 2	1.4	0.7	2.1 ± 0.2	0.93 ± 0.02	3.0 ± 0.5
5	0.58 ± 0.02	2.7 ± 0.3	57 ± 5	1.1	0.8	2.5 ± 0.3	0.97 ± 0.02	1.9 ± 0.3
6	0.57 ± 0.04	2.5 ± 0.5	63 ± 15	1.0	0.8	2.8 ± 0.7	0.97 ± 0.03	1.7 ± 0.5
7	0.61 ± 0.02	3.4 ± 0.2	51 ± 1	1.4	0.7	2.1 ± 0.2	0.93 ± 0.02	2.8 ± 0.3
Tot								24 ± 4

2) RESULTS

The theory reproduces, within data uncertainties, the wave structure and phase speed of the 6-m-amplitude waves (Fig. 11). The theoretical phase speed is $c = 0.53$ m s^{-1}, close to the observed phase speed at midchannel of $c \simeq 0.5$ m s^{-1}. Note that, without background current [i.e., with $V = 0$ in Eq. (8)], the theoretical phase speed for a 6-m-amplitude wave is $c = 0.73$ m s^{-1}. The theoretical horizontal and vertical currents are comparable in magnitude to the observations, but the patterns are qualitatively quite different (Fig. 11). Some complexities of the field measurements cannot be captured with this theory. Nevertheless, the important point for wave reflectance is that the theory satisfactorily reproduces the wave structure and thus the a/L ratio used for calculating the Iribarren number [Eq. (2)].

Concerning the 13-m-amplitude wave, the theory reproduces just as qualitatively well the general wave structure and current patterns (not shown). However, the phase speeds do not match between theory and observations. The theory predicts that a 13-m wave amplitude in this environment would have a phase speed $c = 0.82$ m s^{-1}. The field observations off Pointe-aux-Crêpes rather show phase speeds around 0.5 m s^{-1}, more consistent with 6-m-amplitude waves. It is unclear why there is such a difference. The turbulence observations suggest that this wave is breaking (Fig. 4), an aspect that the DJL theory cannot take into account. Perhaps this explains the phase speed discrepancy.

c. Wave train reflectance

A rough guess of wave train reflectance could be done by realizing that the phase speeds of the reflected waves off Pointe-aux-Crêpes are not much different, to within one significant figure, than the phase speeds of the incoming waves (Table 1). This suggests that the energies of the individual incoming and reflected waves are comparable. Neglecting the fifth reflected wave, which has a much lower phase speed than the other four, a back-of-the-envelope

estimation of the reflectance would give $R = (4$ reflected waves)$/(7$ incoming waves$) = 0.6$.

Along with some assumptions, the DJL theory is now used in combination with the remote phase speed measurements to attempt a more accurate wave train reflectance. The assumptions are as follows:

(i) Given the bended geometry of the channel (Fig. 1), waves approaching the southern flank of Pointe-aux-Crêpes are sheltered from the background current. If the background flow were important, progressive changes in the rays' slopes would be expected because of the no-flow condition across the shoreline, a change that is not observed (Fig. 6). The effect of the background current for waves approaching the coastline, if any, is not discernible and is considered to be within phase speed uncertainties. A similar approach using the DJL theory without background current was used by Klymak and Moum (2003) to infer unobserved properties and energetics of shoaling large-amplitude internal solitary waves of elevation on the Oregon Shelf.

(ii) The shape of the waves approaching or propagating away from the southern flank of Pointe-aux-Crêpes can be accurately predicted by the DJL theory.

(iii) The reflected waves are fully formed as mode-1 solitary waves where their phase speed is measured. Numerical simulations suggest that it takes only

TABLE 2. Mechanical energy of each wave of the reflected wave train (Fig. 6) as inferred from the DJL theory given phase speed measurements and background density profile. See text for definition of variables.

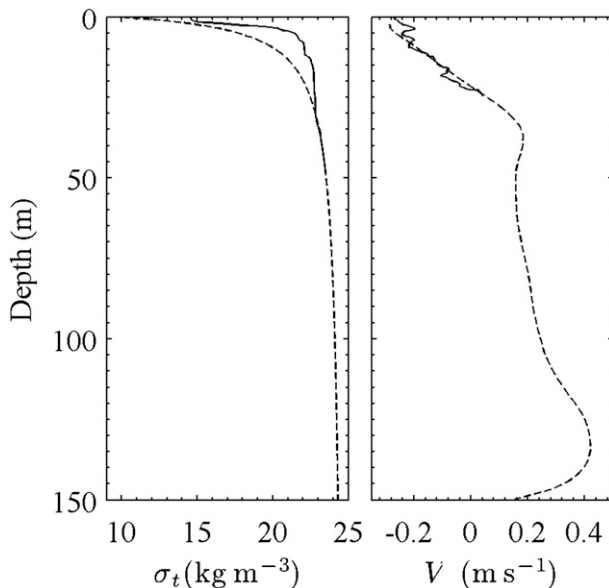| No.	c (m s^{-1})	E_r ($\times 10^4$ J m^{-1})
1	0.65 ± 0.04	4.3 ± 0.9
2	0.61 ± 0.03	2.9 ± 0.5
3	0.66 ± 0.08	5 ± 2
4	0.56 ± 0.04	1.4 ± 0.4
5	0.34 ± 0.03	<0.1
Tot		13 ± 4

FIG. 10. Background (left) density and (right) current profiles used in the DJL model for waves propagating off PC. The solid lines are the observations collected just ahead of the wave train of Fig. 4. When available, the field observations were used; otherwise, data were extrapolated below observational depth (dashed lines). Density measurements were extrapolated using an exponential fit to historical data. Current measurements were extrapolated using results from the numerical circulation model of the fjord from Janes (2008). Note that waves approaching the southern flank of PC were simulated without background current.

a few wavelengths after impact, perhaps 200 m here, for the reflected waves to be fully formed (see, e.g., Lamb and Nguyen 2009, their Fig. 11).

(iv) Waves approach the coastline orthogonally, and focusing or spreading effects are negligible.

(v) All waves, incoming and reflected, have a detectable sea surface signature.

The model setup is as detailed in the previous section, except that $V = 0$ (first assumption) and the total depth is 75 m, which corresponds to the far field isobath along which the wave train approaches the flank of Pointe-aux-Crêpes. From the results, the wave mechanical energy linear density E (J m^{-1}) is calculated as the sum of the available potential energy and kinetic energy as formulated in Lamb (2008) and Lamb and Nguyen (2009).

A series of 34 simulations was carried out, covering a range of phase speeds from about 0.5 to 0.9 m s^{-1}. From these simulations, wave amplitudes, horizontal length scales, and energies were extracted. Discrete theoretical relationships between wave amplitude a and phase speed c, as well as between horizontal length scale L and c (Fig. 12), were interpolated at observed phase speeds to provide the characteristics (a and L) of each wave that

composes the incoming wave train (Table 1). From these, the Iribarren number ξ was estimated given the bottom slope of the southern flank of Pointe-aux-Crêpes along the wave propagation path $s = 0.55 \pm 0.02$ (Table 1).

In comparison to the total depth, $H = 75$ m, and to the thickness of the undisturbed surface layer, $h_1 = 2.5$ m (Fig. 5), the incoming waves are short ($\lambda \equiv L/H < 1$) and have large amplitudes ($\alpha \equiv a/h_1 > 1$). In comparison to the wave slope, the bottom slope of the southern flank of Pointe-aux-Crêpes is steep ($\xi > 1$).

Similarly, wave mechanical energies were determined from observed phase speeds (Fig. 13). The incoming wave train energy is estimated as $E_i = (24 \pm 4) \times 10^4$ J m^{-1} (Table 1). A similar analysis was carried out for the reflected waves, which provided a total reflected wave train energy $E_r = (13 \pm 4) \times 10^4$ J m^{-1} (Table 2). Comparing these values suggests a wave train reflectance $R = E_r/E_i = 0.5 \pm 0.2$.

5. Discussion

The wave train reflectance, estimated using observed phase speed, density profile, and the DJL theory, is $R = 0.5 \pm 0.2$. By comparison, the wave train reflectance estimated from applying parameterization (1) to each individual wave of the wave train is about 2 times higher with $R_{BK} = 0.9$ (Table 1). For oceanographers interested in quantifying wave-induced boundary mixing, this is an important difference because errors in R can lead to larger errors in mixing estimates. For example, the increase in background potential energy due to shoaling waves on internal beaches can be taken as

$$\Delta P = \Gamma(1 - R)E_i, \quad (10)$$

where $\Gamma \approx 0.15$ is the fraction of the energy lost to turbulence used for mixing buoyancy (Helfrich 1992; Michallet and Ivey 1999). Using $R_{BK} = 0.9$ in (10) leads to an estimate of wave-induced boundary mixing 5 times lower than if using $R = 0.5$ (see also a similar discussion in Bourgault and Kelley 2007).

Why such a difference between our inferred reflectance R and that predicted by parameterization (1) besides the possibility of the analysis being based on incorrect assumptions? One hypothesis is that parameterization (1) was developed for single impinging internal solitary waves, a situation rarely observed in natural environments. It could be that, because of wave interactions during shoaling, the reflectance of a solitary wave train is significantly different than the reflectance resulting from a series of well separated waves. This is consistent with the laboratory experiment of Boegman et al. (2005b) where they reported lower reflectance for
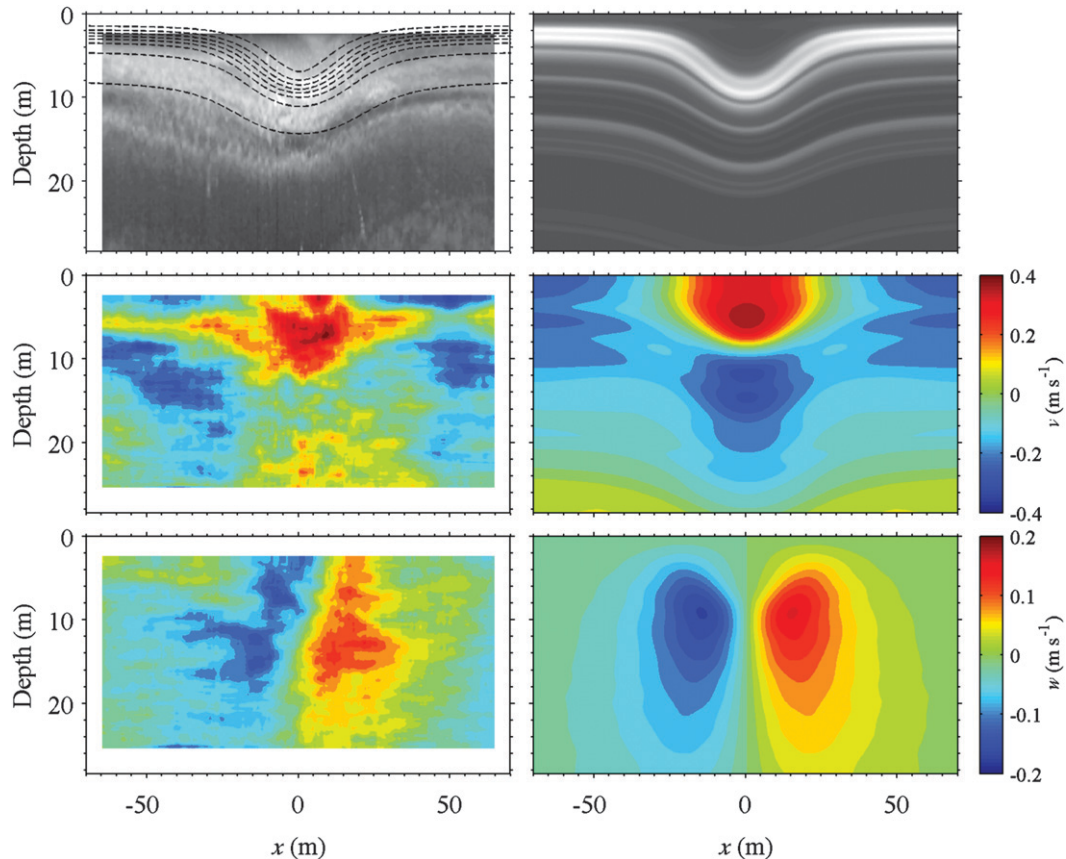
FIG. 11. Comparison between (left) field measurements and (right) results from the DJL theory for the second wave of Fig. 4. (top left) The observed echogram on top of which the isopycnals from the DJL theory are plotted (dashed contour lines) for comparison. (top right) The logarithm of the vertical density gradient. This quantity is used to mimic the echogram for qualitative comparison. The (middle) horizontal v and (bottom) vertical w current components. The measurements were Doppler corrected knowing the boat drift velocity, from GPS measurements, and wave phase speed, from the georectified photography.

shoaling internal wave trains than would be anticipated for single waves.

Another hypothesis that may explain the difference is that the laboratory and numerical experiments underlying the parameterization in (1) are geometrically dissimilar to the wave-boundary conditions prevailing in the Saguenay Fjord. These experiments examined long incoming waves, (i.e., waves for which $\lambda > 1$). Michallet and Ivey (1999), as well as Bourgault and Kelley (2007) and Lamb and Nguyen (2009), explored the range $1.0 \leq \lambda \leq 3.7$, and Chen et al. (2007) explored $1.0 \leq \lambda \leq 3.0$. The waves observed in this study are characterized with $\lambda < 1$ (Table 1). Because short solitary waves have different properties than long solitary waves, in shape and current structure (Ostrovsky and Stepanyants 1989), it is possible that they also have different reflectance behavior. For example, long waves are affected by the shoaling bottom along the entire length of the slope, whereas, for the same

bathymetry, short waves become affected by the shoaling bottom only farther up the slope.

The λ parameter is not the only one that differs between the laboratory-scale experiments and the field observations reported here. The combination of large-amplitude waves ($\alpha > 1$) and steep slopes ($\xi > 1$), a situation that characterizes the waves in the Saguenay Fjord, has not been addressed by Michallet and Ivey (1999) and consequently by Bourgault and Kelley (2007) and Lamb and Nguyen (2009). This is illustrated in Fig. 14, which shows the ξ–α parameter space explored by Michallet and Ivey (1999) in comparison to the condition prevailing in the Saguenay Fjord. The laboratory experiments have examined large-amplitude waves ($\alpha > 1$) shoaling on gentle slopes ($\xi > 1$) as well as small-amplitude waves ($\alpha > 1$) shoaling on steep slopes ($\xi > 1$), but cases of large-amplitude waves ($\alpha > 1$) shoaling on steep slopes ($\xi > 1$) have not been explored.
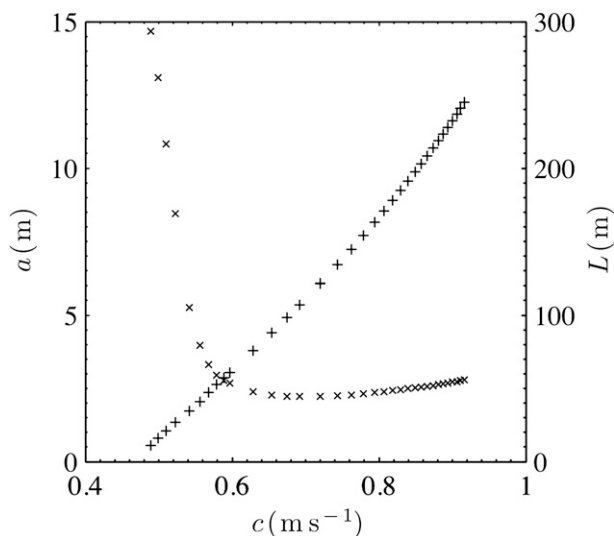
FIG. 12. Theoretical relationship between amplitude a (denoted by plus symbols), wave horizontal length scale L (denoted by crisscrosses), and wave phase speed c. These functions are used to infer wave amplitude and length scale from the phase speed measurements.

FIG. 13. Theoretical relationship between wave mechanical energy E and phase speed c.

According to Boegman et al. (2005a, their Table 2), occurrences of large-amplitude waves shoaling on steep slopes may not be common in coastal environments like lakes, shelves and bays (Fig. 14). However, fjord-like environments with steep sidewalls and thin surface layers, like the Saguenay Fjord or Knight Inlet (Cummins et al. 2003), are likely characterized by such situations (Fig. 14).

Another important difference between existing laboratory-scale results on internal solitary wave reflectance and the Saguenay Fjord is the roughness of the bottom topography. Current understanding is based on the reflectance of waves on smooth slopes. The sidewalls of the Saguenay Fjord are characterized with irregular rocky cliffs with large cracks and boulders. Reflectance may be expected to decrease with increasing bottom roughness, but this aspect remains to be studied.

Finally, the Reynolds number significantly differs between the laboratory-scale experiments (Re $\sim 10^3$) and the field observations reported here (Re $\sim 10^8$). However, it is unlikely that this dissimilarity explains the lower reflectance inferred from the field measurements because the numerical results of Lamb and Nguyen (2009) suggest that higher Reynolds number situations lead to higher reflectance.

6. Conclusions

Our analysis, based on field observations, a nonlinear theory, and some assumptions, provides a wave train reflectance $R = 0.5 \pm 0.2$. This is about 0.4 lower than the
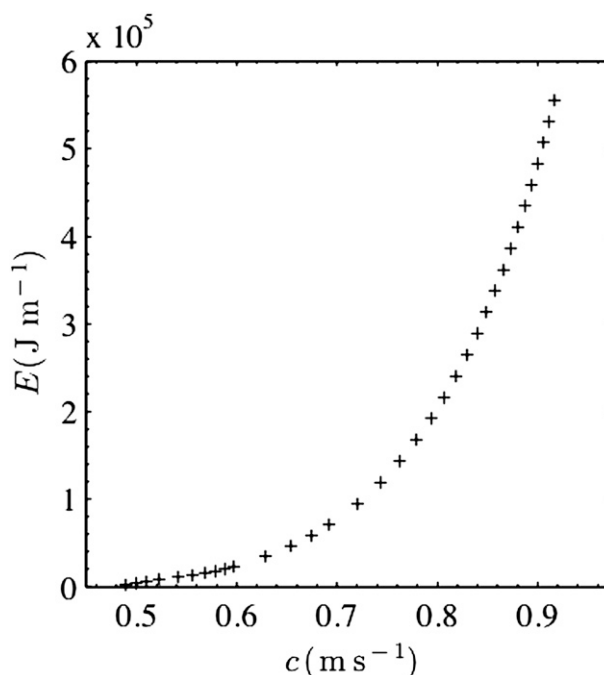
Bourgault and Kelley (2007) parameterization would suggest, which is based on reflections of single solitary waves. We have attributed this difference to a number of dissimilarities between natural fjord-like environments and laboratory-scale settings upon which current understanding of internal solitary wave reflectance is based. Our discussion suggests that we should perhaps refrain from using the Bourgault and Kelley (2007) parameterization [Eq. (1)], as well as any other existing laboratory-based findings for lone waves (e.g., Helfrich 1992; Michallet and Ivey 1999; Chen et al. 2007; Lamb and Nguyen 2009), to infer the reflective and mixing properties of steep natural boundaries ($\xi > 1$) subject to large-amplitude ($\alpha > 1$) and short ($\lambda < 1$) internal solitary wave trains.

More fundamental research is needed to address these situations that characterize fjord-like systems. Equally important is to collect new field measurements that would allow the reflectance of internal solitary wave trains off natural slopes to be directly calculated. Fjord-like environments with steep boundaries (i.e., with $\xi > 1$) might be ideal locations to attempt such measurements because the reflected waves may be detectable, as shown here, as opposed to gentle slope environments where the reflected signal may prove to be difficult to extract from measurements.

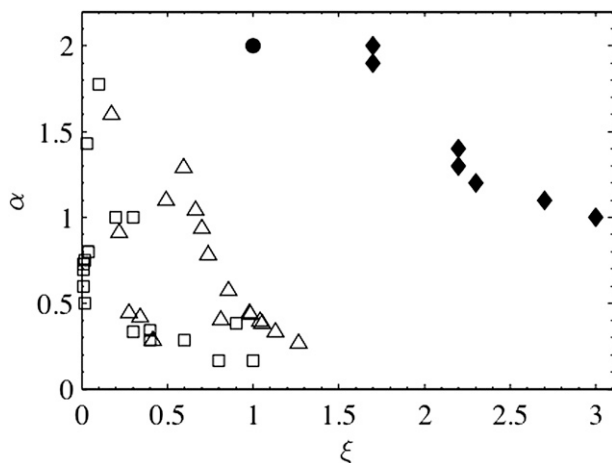FIG. 14. The ξ–α parameter space explored by Michallet and Ivey (1999) and related studies (triangles; from their Table 1), compared to field observations from various coastal environments (squares; from Table 2 in Boegman et al. 2005a) and to observations made in this study in the Saguenay Fjord (filled diamonds). Conditions prevailing in Knight Inlet (filled circles) are similar to those in the Saguenay Fjord as estimated from Figs. 1 and 7 of Cummins et al. (2003).

REFERENCES

Bélanger, C., 2003: Observation and modelling of a renewal event in the Saguenay Fjord. Ph.D. thesis, Université du Québec à Rimouski, 235 pp.

Boegman, L., G. N. Ivey, and J. Imberger, 2005a: The degeneration of internal waves in lakes with sloping topography. *Limnol. Oceanogr.,* **50,** 1620–1637.

——, ——, and ——, 2005b: The energetics of large-scale internal wave degeneration in lakes. *J. Fluid Mech.,* **531,** 159–180.

Bourgault, D., 2008: Shore-based photogrammetry of river ice. *Can. J. Civ. Eng.,* **35,** 80–86.

——, and D. E. Kelley, 2003: Wave-induced boundary mixing in a partially mixed estuary. *J. Mar. Res.,* **61,** 553–576.

——, and ——, 2004: A laterally averaged nonhydrostatic ocean model. *J. Atmos. Oceanic Technol.,* **21,** 1910–1924.

——, and ——, 2007: On the reflectance of uniform slopes for normally incident interfacial solitary waves. *J. Phys. Oceanogr.,* **37,** 1156–1162.

——, ——, and P. S. Galbraith, 2005: Interfacial solitary wave run-up in the St. Lawrence Estuary. *J. Mar. Res.,* **63,** 1001–1015.

——, M. D. Blokhina, R. Mirshak, and D. E. Kelley, 2007: Evolution of a shoaling internal solitary wavetrain. *Geophys. Res. Lett.,* **34,** L03601, doi:10.1029/2006GL028462.

——, D. E. Kelley, and P. S. Galbraith, 2008: Turbulence and boluses on an internal beach. *J. Mar. Res.,* **66,** 563–588.

Chen, C.-Y., J. R.-C. Hsu, M.-H. Cheng, H.-H. Chen, and C.-F. Kuo, 2007: An investigation on internal solitary waves in a two-layer fluid: Propagation and reflection from steep slopes. *Ocean Eng.,* **34,** 171–184, doi:10.1016/j.oceaneng.2005.11.020.

Cummins, P. F., S. Vagle, L. Armi, and D. M. Farmer, 2003: Stratified flow over topography: Upstream influence and generation of nonlinear internal waves. *Proc. Roy. Soc. London,* **459A,** 1467–1487.

Denman, K. L., and A. E. Gargett, 1988: Multiple thermoclines are barriers to vertical exchange in the subarctic Pacific during SUPER, May 1984. *J. Mar. Res.,* **46,** 77–103.

Farmer, D. M., and L. Armi, 1999: The generation and trapping of internal solitary waves over topography. *Science,* **283** (5398), 188–190.

Galbraith, P. S., and D. E. Kelley, 1996: Identifying overturns in CTD profiles. *J. Atmos. Oceanic Technol.,* **13,** 688–702.

Gargett, A. E., T. R. Osborn, and P. W. Nasmyth, 1984: Local isotropy and the decay of turbulence in a stratified fluid. *J. Fluid Mech.,* **144,** 231–280.

Helfrich, K. R., 1992: Internal solitary wave breaking and run-up on a uniform slope. *J. Fluid Mech.,* **243,** 133–154.

——, and W. K. Melville, 2006: Long nonlinear internal waves. *Annu. Rev. Fluid Mech.,* **38,** 395–425.

Janes, D. C., 2008: Sill processes in the Saguenay Fjord. M.S. thesis, Dept. of Physics and Physical Oceanography, Memorial University of Newfoundland, 78 pp.

Klymak, J. M., and J. N. Moum, 2003: Internal solitary waves of elevation advancing on a shoaling shelf. *Geophys. Res. Lett.,* **30,** 2045, doi:10.1029/2003GL017706.

——, and M. C. Gregg, 2004: Tidally generated turbulence over the Knight Inlet sill. *J. Phys. Oceanogr.,* **34,** 1135–1151.

Lamb, K. G., 2002: A numerical investigation of solitary internal waves with trapped coreformed via shoaling. *J. Fluid Mech.,* **451,** 109–144, doi:10.1017/S002211200100636X.

——, 2008: On the calculation of the available potential energy of an isolated perturbation in a density-stratified fluid. *J. Fluid Mech.,* **597,** 415–427, doi:10.1017/S0022112007009743.

——, and V. T. Nguyen, 2009: Calculating energy flux in internal solitary waves with an application to reflectance. *J. Phys. Oceanogr.,* **39,** 559–580.

Macoun, P., and R. Lueck, 2004: Modeling the spatial response of the airfoil shear probe using different sized probes. *J. Atmos. Oceanic Technol.,* **21,** 284–297.

Michallet, H., and G. N. Ivey, 1999: Experiments on mixing due to internal solitary waves breaking on uniform slopes. *J. Geophys. Res.,* **104** (C6), 13 467–13 477.

Miles, J., 1961: On the stability of heterogeneous shear flows. *J. Fluid Mech.,* **10,** 496–508.

Moum, J. N., M. C. Gregg, R. C. Lien, and M. E. Carr, 1995: Comparison of turbulence kinetic energy dissipation rate estimates from two ocean microstructure profilers. *J. Atmos. Oceanic Technol.,* **12,** 346–366.

——, D. M. Farmer, E. L. Shroyer, W. D. Smyth, and L. Armi, 2007a: Dissipative losses in nonlinear internal waves propagating across the continental shelf. *J. Phys. Oceanogr.,* **37,** 1989–1995.

——, J. M. Klymak, J. Nash, A. Perlin, and W. D. Smyth, 2007b: Energy transport by nonlinear internal waves. *J. Phys. Oceanogr.,* **37,** 1968–1988.

Oakey, N. S., and J. A. Elliott, 1982: Dissipation within the surface mixed layer. *J. Phys. Oceanogr.,* **12,** 171–185.

Ostrovsky, L. A., and Y. A. Stepanyants, 1989: Do internal solitons exist in the ocean? *Rev. Geophys.,* **27,** 292–319.

Pawlowicz, R., 2003: Quantitative visualization of geophysical flows using digital oblique time-lapse imaging. *IEEE J. Oceanic Eng.,* **28,** 699–710.

Peters, H., 1997: Observations of stratified turbulent mixing in an estuary: Neap-to-spring variations during high river flow. *Estuarine Coastal Shelf Sci.,* **45,** 69–88.

Scotti, A., and J. Pineda, 2004: Observation of very large and steep internal waves of elevation near the Massachusetts coast. *Geophys. Res. Lett.,* **31,** L22307, doi:10.1029/2004GL021052.

Stacey, M. W., and Y. Gratton, 2001: The energetics, and tidally induced reverse renewal in a two-silled fjord. *J. Phys. Oceanogr.,* **31,** 1599–1615.

Stastna, M., and K. G. Lamb, 2002: Large fully nonlinear internal solitary waves: The effect of background current. *Phys. Fluids,* **14,** 2987–2999.

Thorpe, S. A., 2005: *The Turbulent Ocean.* Cambridge University Press, 439 pp.

Turkington, B., A. Eydeland, and S. Wang, 1991: A computational method for solitary internal waves in a continuously stratified fluid. *Stud. Appl. Math.,* **85,** 93–127.

Wallace, B. C., and D. L. Wilkinson, 1988: Run-up of internal waves on a gentle slope in a two-layered system. *J. Fluid Mech.,* **191,** 419–442.

Wesson, J. C., and M. C. Gregg, 1994: Mixing at Camarinal sill in the Strait of Gibraltar. *J. Geophys. Res.,* **99** (C5), 9847–9878.